An Algorithm Using Visible and 1.38-μm Channels to Retrieve Cirrus Cloud Reflectances From Aircraft and Satellite Data

Bo-Cai Gao, Ping Yang, *Fellow, IEEE*, Wei Han, Rong-Rong Li, and Warren J. Wiscombe

***Abstract*—The Moderate Resolution Imaging Spectro-Radiometer (MODIS) on the Terra Spacecraft has a channel near 1.38 μm for remote sensing of high clouds from space. The implementation of this channel on MODIS was primarily based on previous analysis of hyperspectral imaging data collected with the Airborne Visible Infrared Imaging Spectrometer (AVIRIS). In this paper, we describe an algorithm to retrieve cirrus bidirectional reflectance using channels near 0.66 and 1.38 μm. It is shown that the apparent reflectance of the 1.38-μm channel is essentially the bidirectional reflectance of cirrus clouds attenuated by the absorption of water vapor above cirrus clouds. A practical algorithm based on the scatterplot of 1.38-μm channel apparent reflectance versus 0.66-μm channel apparent reflectance has been developed to scale the effect of water vapor absorption so that the true cirrus reflectance in the visible spectral region can be obtained. To illustrate the applicability of the present algorithm, results for cirrus reflectance retrievals from AVIRIS and MODIS data are shown. The derived cirrus reflectance in the spectral region of 0.4–1 μm can be used to remove cirrus contamination in a satellite image obtained at a visible channel. An example of such application is shown. The spatially averaged cirrus reflectances derived from MODIS data can be used to establish global cirrus climatology, as is demonstrated by a sample global cirrus reflectance image.**

***Index Terms*—Atmosphere, cirrus clouds, remote sensing.**

I. Introduction

CIRRUS CLOUDS normally exist in the upper troposphere and sometimes extend to the stratosphere. Recent observations [20], [21] have shown that cirrus cover can be as high as 30% of the globe; in particular, the occurrence of cirrus clouds inferred from satellite data is normally larger than 50% over mid-latitude and tropical regions [1]. A number of ground observations at various urban airports indicate that high cloud cover has doubled over the past 40 years [3]. The increase of high clouds is partially correlated to the formation of contrails produced by jet airplanes [15], which have been significantly increased. Unlike warm water clouds, cirrus clouds are almost exclusively composed of nonspherical ice crystals with various sizes and shapes. At this point, the effect of cirrus clouds on the earth–atmosphere energy budget is far from being well understood. Cirrus clouds have been identified as one of the most uncertain components in weather and climate studies [12], [13], [19].

The optical properties of cirrus clouds are of major concerns in remote sensing applications. This is because the scattering and absorption of ice crystals within cirrus/contrail clouds can substantially modulate the radiative transfer [11] in the atmosphere. To develop reliable and accurate algorithms for retrieving surface products [such as the normalized difference vegetation index (NDVI)] or oceanic products (e.g., the concentration of chlorophyll) from satellite radiance data, the removal of atmosphere effects (the so-called atmospheric correction) must be carried out properly [17]. Otherwise, the retrieved surface/oceanic products may be incorrect and misleading. Cirrus contamination should be an important factor to be considered in atmospheric correction processes. The importance for the correction of cirrus effect has been illustrated for retrieving reliable NDVI values [7] associated with scenes slightly contaminated by cirrus clouds.

Through analysis of hyperspectral imaging data collected by the Airborne Visible Infrared Imaging Spectrometer (AVIRIS) instrument [16] from an ER-2 aircraft at 20-km altitude, it was found that narrow channels near the center of the strong 1.38-μm water vapor band are very effective in detecting thin cirrus clouds [4], [6]. Based on this observation, a channel centered near 1.38 μm was selected [5] and implemented on the Moderate Resolution Imaging SpectroRadiometer (MODIS) instrument. With this new channel, the measurements from the MODIS instrument on the Terra Spacecraft can be used for global observations of cirrus clouds.

The intent of this study is to develop an algorithm to derive cirrus cloud reflectances using visible and 1.38-μm channels. In Section II, we present the basic principle for deriving cirrus cloud reflectance using the two channels. In Section III, we present examples for cirrus reflectance derivations from AVIRIS and MODIS data. Finally, conclusions are given in Section IV.

II. Retrieval of Cirrus Cloud Reflectance Using Visible and 1.38-μm Bands

A. Apparent Cirrus Reflectance Viewed From Space

Cirrus clouds are located generally at an altitude above 7 km in the mid-latitude and 9 km in the tropical region [11]. Contrails

Manuscript received November 8, 2001; revised May 22, 2002. This research was supported by the National Aeronautics and Space Administration EOS MODIS project and by the U.S. Office of Naval Research.

B.-C. Gao is with the Remote Sensing Division, Naval Research Laboratory, Washington, DC 20375 USA (e-mail: gao@nrl.navy.mil).

P. Yang is with the Department of Atmospheric Sciences, Texas A&M University, College Station, TX 77843 USA.

W. Han is with the Publication/Information Technology Division, American Chemistry Society, Washington, DC 20036 USA.

R.-R. Li is with the Science Systems and Applications, Inc., Code 913, NASA Goddard Space Flight Center, Greenbelt, MD 20771 USA.

W. J. Wiscombe is with the Climate and Radiation Branch, NASA Goddard Space Flight Center, Greenbelt, MD 20771 USA.

Publisher Item Identifier 10.1109/TGRS.2002.802454.

0196-2892/02$17.00 © 2002 IEEE

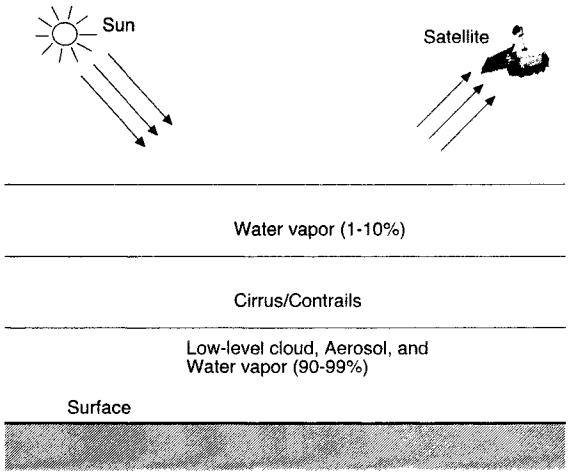

Fig. 1. The solar and view geometry as well as atmosphere-earth configuration for the bidirectional reflectance of cirrus clouds from satellite observation.

are found mainly in the stratosphere at the altitude of air traffic. The low- and middle-level water clouds, major aerosol loading, and 90%–99% of the atmospheric water vapor are located below cirrus/contrails. The altitude data collected by various investigators for cirrus clouds, which have been compiled in [2], indicate that these clouds are normally above 10 km. Water vapor above cirrus/contrail is normally 1%–10%, which will produce a nonnegligible effect for strong absorptive bands, including the one centered at 1.38 μm. For the retrieval of cirrus/contrail clouds based on aircraft and satellite measurements, the atmosphere-earth system can be viewed as being composed of three layers, as is shown in Fig. 1. The uppermost layer is the water vapor layer above cirrus/contrails; the middle layer is cirrus or contrails; and bottom layer contains low-level water clouds, aerosols, water vapor in the boundary layer and lower troposphere, and the surface. In this manner, the cirrus layer is assumed to be located above a "virtual surface" that includes the effects of scattering and absorption by molecules of various gases (including the low-level water vapor), aerosols, and low- and middle-level clouds, as well as the reflection from the earth surface [6]. Based on the fundamental principles of radiative transfer process, the apparent reflection of the earth–atmosphere systems viewed from a satellite platform can be expressed as

$$\begin{aligned} r(\lambda;\mu_0,\phi_0;\mu,\phi) &= t_w(\lambda,\mu_0)\, r_c(\lambda,\mu_0,\phi_0,\mu,\phi)\, t_w(\lambda,\mu) \\ &\quad + t_w(\lambda,\mu_0)\exp\left(\frac{-\tau}{\mu_0}\right)\frac{r_s(\lambda,\mu_0,\phi_0)}{1-\bar{r}_c^*(\lambda)\bar{r}_s(\lambda)} \\ &\quad \cdot\left[\exp\left(\frac{-\tau}{\mu}\right)+t_c^*(\lambda,\mu,\phi)\right] t_w(\lambda,\mu) \\ &\quad + t_w(\lambda,\mu_0)\, t_c(\lambda,\mu_0,\phi_0)\frac{\bar{r}_s(\lambda)}{1-\bar{r}_c^*(\lambda)\bar{r}_s(\lambda)} \\ &\quad \cdot\left[\exp\left(\frac{-\tau}{\mu}\right)+t_c^*(\lambda,\mu,\phi)\right] t_w(\lambda,\mu), \end{aligned} \tag{1}$$

where λ is wavelength, while τ is the optical thickness of the cirrus cloud. The two parameters $\mu_0 = \cos\theta_0$ and $\mu = \cos\theta$ that are for the angular geometry of the radiation transfer are for the sun zenith angle (θ_0) and satellite zenith angle (θ), respectively. The azimuth angles ϕ_0 and ϕ are associated with θ_0 and θ, respectively. t_w is the transmittance associated with the amount of water vapor above the cirrus/contrails. $r_c(\lambda,\mu_0,\phi_0,\mu,\phi)$ is the bidirectional reflectance of cirrus clouds for the radiation that impinges from above. $\bar{r}_c^*(\lambda)$ is the spherical albedo of the clouds for upwelling radiation, given by

$$\bar{r}_c^*(\lambda) = \frac{1}{\pi^2}\int_0^{2\pi}\int_0^1\int_0^{2\pi}\int_0^1 r_c^*(\lambda,\mu_0,\phi_0,\mu,\phi)\, d\phi_0\mu_0 d\mu_0 d\phi\mu d\mu. \tag{2}$$

Note that the asterisks in (1) and (2) indicate that the corresponding quantities are for upwelling radiation. The plane albedo of the "virtual surface" $r_s(\lambda,\mu_0,\phi_0)$ is given by the corresponding bidirectional reflectance $r_s(\lambda,\mu_0,\phi_0,\mu,\phi)$ via the following relationship:

$$r_s(\lambda,\mu_0,\phi_0) = \frac{1}{\pi}\int_0^{2\pi}\int_0^1 r_s(\lambda,\mu_0,\phi_0,\mu,\phi)\,\mu d\phi d\mu \tag{3}$$

and the spherical albedo of the "virtual surface" is given by

$$\bar{r}_s(\lambda) = \frac{1}{\pi}\int_0^{2\pi}\int_0^1 r_s(\lambda,\mu_0,\phi_0)\,\mu_0 d\phi_0 d\mu_0. \tag{4}$$

In (1), the diffused transmittances of the cirrus cloud for downward and upwelling radiation are given by

$$t_c(\lambda,\mu_0,\phi_0) = \frac{1}{\pi}\int_0^{2\pi}\int_0^1 t_c(\lambda,\mu_0,\phi_0,\mu,\phi)\,\mu d\phi d\mu \tag{5a}$$

$$t_c^*(\lambda,\mu,\phi) = \frac{1}{\pi}\int_0^{2\pi}\int_0^1 t_c^*(\lambda,\mu',\phi',\mu,\phi)\mu' d\phi' d\mu'. \tag{5b}$$

Note that (1) implies a Lambertian feature for the "virtual surface" for the photons that have undergone the single and multiple scattering within cirrus clouds or the reflection between cirrus clouds and the "virtual surface." In reality, the reflectance of the surface depends upon the direction of incident radiation, the surface radiative properties, and the direction from which the surface is being viewed. The surface reflectance in this case should be characterized by the bidirectional reflectance distribution function (BRDF) [10]. The surface BRDF will have little effect, if not at all, on 1.38-μm apparent reflectance of cirrus clouds because the radiation reflected by the surface is essentially absorbed by water vapor below the cirrus clouds. However, the effect of the surface BRDF on the apparent reflectance of the "virtual surface" at the 0.66-μm channel may not be negligible. It is a quite challenging issue to accurately and quantitatively account for the effect of surface BRDF. For simplicity, in the present algorithm, we ignore this effect.

The proceeding equations are monochromatic, i.e., for a single wavelength. In airborne and satellite measurements, the instruments are operated at spectral bands with certain wavelength intervals. Let the spectral width for a given band be $\Delta\lambda$ with the band center at λ_0, and let the product of the instrument response function and solar spectral irradiance be $S(\lambda)$. Thus, from (1), the band-averaged apparent reflectance is given by (6a)–(6f), shown at the bottom of the next page. Note that T_{w,λ_0} in (6c) is the two-way transmittance [6] associated with the absorption of water vapor above the cirrus layer. In

(6c), decoupling of the band-averaged two-way transmittance of water vapor and the cirrus reflectance is allowed by the fact that the latter has a weak spectral dependence for a narrow spectral band of the instrument. In (6f), the terms associated with reflection of the "virtual surface" $r_s(\lambda, \mu_0, \phi_0)$ and $\bar{r}_s(\lambda)$ implicitly include the absorption effect of water vapor below cirrus clouds. Because water vapor is strongly absorptive at wavelengths near 1.38 μm and since a substantial amount of water vapor is within the "virtual surface," the reflection of the "virtual surface" is essentially zero at this band [4], i.e.,

$$\begin{aligned} r_s(\lambda, \mu_0, \phi_0)\big|_{\lambda \approx 1.38\ \mu\text{m}} &\cong 0 \\ \bar{r}_s(\lambda)\big|_{\lambda \approx 1.38\ \mu\text{m}} &\cong 0. \end{aligned} \tag{7}$$

Thus, for a spectral band centered at $\lambda_0 = 1.38\ \mu$m, we have

$$r_{1.38}(\mu_0, \phi_0, \mu, \phi) = T_{w,1.38}(\mu_0, \mu)\, r_{c,1.38}(\mu_0, \phi_0, \mu, \phi). \tag{8}$$

At a visible wavelength, the absorption of water vapor is negligible. Thus, the two-way transmittance of water vapor is essentially unity, regardless of solar and view geometry, i.e., $T_{w,0.66}(\mu_0, \mu) = 1$. Additionally, the contribution of the reflection of the "virtual surface" to the apparent reflectance observed from an airborne or satellite instrument is significant at a visible band. For this reason, we have

$$r_{0.66}(\mu_0, \phi_0, \mu, \phi) = r_{c,0.66}(\mu_0, \phi_0, \mu, \phi) + b_{0.66}(\mu_0, \phi_0, \mu, \phi). \tag{9}$$

It has been shown that there is a quasi linear relationship for reflectance of cirrus clouds at 0.66- and 1.38-μm bands found [6], i.e.,

$$r_{c,1.38}(\mu_0, \phi_0, \mu, \phi) = a r_{c,0.66}(\mu_0, \phi_0, \mu, \phi) \tag{10}$$

where a is a quasi constant that is smaller than 1 because of the weak absorption of ice crystals at 1.38 μm. It has been found from theoretical calculation that the single-scattering properties of ice crystals have little spectral variation for wavelengths between 0.4–1.0 μm [22]. Therefore, we have

$$r_c(\lambda, \mu_0, \phi_0, \mu, \phi) \approx r_{c,0.66}(\mu_0, \phi_0, \mu, \phi) \text{ for } \lambda \in [0.4, 1.0\ \mu\text{m}]. \tag{11}$$

Equations (9)–(11) provide the theoretical basis for retrieving the reflectance of cirrus clouds at visible wavelengths.

B. Two-Band Algorithm for Retrieving Cirrus Reflectance at Visible Spectrum

In this study, we use a visible band centered at 0.66 μm and near infrared band centered at 1.38 μm to retrieve cirrus reflectance at the visible spectrum. These images at two bands are available from AVIRIS and MODIS measurements. The former instrument (which is flown on a NASA ER-2 aircraft at an altitude of 20 km) has 224 contiguous 10-nm-wide spectral bands. The ground spatial resolution of AVIRIS is 20 m with the swath width about 10 km. A typical AVIRIS image contains 614 $\times$ 512 pixels. MODIS is a 36-channel scanning radiometer on the EOS Terra platform [8]. The widths for MODIS 0.66-μm and 1.38-μm bands are 0.050 and 0.030 μm, respectively. The typical size for MODIS Level-1b images used in this study is 1354×2030 pixels, and the spatial sizes of the images are about 2000 km in the direction along the satellite orbital track and 2800 km in the cross-track direction.

The fundamental equation for retrieving cirrus reflectance can be obtained by substituting (10) into (8), i.e.,

$$r_{1.38}(\mu_0, \phi_0, \mu, \phi) = \Gamma r_{c,0.66}(\mu_0, \phi_0, \mu, \phi) \tag{12a}$$

or

$$r_{1.38}(\mu_0, \phi_0, \mu, \phi) \approx \Gamma r_c(\lambda, \mu_0, \phi_0, \mu, \phi), \quad \lambda \in [0.4, 1.0\ \mu\text{m}] \tag{12b}$$

where $\Gamma = a T_{w,\lambda_0}$ in which $T_{w,1.38}$ and a are defined in (6d) and (10), respectively. Since $r_{1.38}(\mu_0, \phi_0, \mu, \phi)$ is from measurement, it will be straightforward to derive the cirrus

---

$$r_{\lambda_0}(\mu_0, \phi_0, \mu, \phi) = \langle t_w(\lambda, \mu_0)\, r_c(\mu_0, \phi_0, \mu, \phi)\, t_w(\lambda, \mu_0) \rangle + b_{\lambda_0}(\mu_0, \phi_0, \mu, \phi) \tag{6a}$$

where

$$r_{\lambda_0}(\mu_0, \phi_0, \mu, \phi) = \frac{1}{\Delta\lambda} \int_{\lambda_0 - \Delta\lambda/2}^{\lambda_0 + \Delta\lambda/2} r(\lambda, \mu_0, \phi_0, \mu, \phi)\, s(\lambda) d\lambda \tag{6b}$$

$$\begin{aligned} \langle t_w(\lambda, \mu_0)\, r_c(\mu_0, \phi_0, \mu, \phi)\, t_w(\lambda, \mu_0) \rangle &= \frac{1}{\Delta\lambda} \int_{\lambda_0 - \Delta\lambda/2}^{\lambda_0 + \Delta\lambda/2} t_w(\lambda, \mu_0)\, r_c(\mu_0, \phi_0, \mu, \phi)\, t_w(\lambda, \mu_0)\, S(\lambda) d\lambda \\ &\approx T_{w,\lambda_0}(\mu, \mu_0)\, r_{c,\lambda_0}(\mu_0, \phi_0, \mu, \phi) \end{aligned} \tag{6c}$$

$$T_{w,\lambda_0}(\mu, \mu_0) = \frac{1}{\Delta\lambda} \int_{\lambda_0 - \Delta\lambda/2}^{\lambda_0 + \Delta\lambda/2} t_w(\lambda, \mu) t_w(\lambda, \mu_0) s(\lambda) d\lambda \tag{6d}$$

$$r_{c,\lambda_0}(\mu_0, \phi_0, \mu, \phi) = \frac{1}{\Delta\lambda} \int_{\lambda_0 - \Delta\lambda/2}^{\lambda_0 + \Delta\lambda/2} r_c(\lambda, \mu_0, \phi_0, \mu, \phi)\, s(\lambda) d\lambda \tag{6e}$$

$$\begin{aligned} b_{\lambda_0}(\mu_0, \phi_0, \mu, \phi) = \frac{1}{\Delta\lambda} \int_{\lambda_0 - \Delta\lambda/2}^{\lambda_0 + \Delta\lambda/2} t_w(\lambda, \mu_0) \Bigg\{ \Bigg[\exp\left(\frac{-\tau}{\mu_0}\right) \frac{r_s(\lambda, \mu_0, \phi_0)}{1 - \bar{r}_c^* \bar{r}_s} + t_c(\lambda, \mu_0, \phi_0) \\ \cdot \frac{\bar{r}_s(\lambda)}{1 - \bar{r}_c^*(\lambda) \bar{r}_s} \left[\exp\left(-\frac{\tau}{\mu}\right) \right] \Bigg\} t_c^*(\lambda, \mu, \phi) \Bigg] t_w(\lambda, \mu) s(\lambda) d\lambda \end{aligned} \tag{6f}$$

reflectance $r_c(\lambda, \mu_0, \phi_0, \mu, \phi)|_{\lambda=0.4\text{–}1.38\ \mu\text{m}}$ if the quantity Γ is known. Thus, successful retrieval of cirrus reflectance depends, essentially, on how to reliably derive Γ. Evidently, there are two unknowns in (12b): Γ and $r_c(\lambda, \mu_0, \phi_0, \mu, \phi)|_{\lambda=0.4\text{–}1.38\ \mu\text{m}}$. As is obvious from a mathematical common sense, it is impossible to derive the two unknowns using one equation, or the one-band spectral information provided measurement at 1.38-μm. To overcome this difficulty, the spectral information at an additional band is required. For this reason, we use both the 0.66- and 1.38-μm bands. It is evident from (9) and (12a) that the apparent reflectance at the 0.66- and 1.38-μm bands can be related in the form

$$r_{1.38}(\mu_0, \phi_0, \mu, \phi) = \Gamma r_{0.66}(\mu_0, \phi_0, \mu, \phi) + d \tag{13}$$

where $d = -\Gamma b_{0.66}(\mu_0, \phi_0, \mu, \phi)$ in which $b_{0.66}(\mu_0, \phi_0, \mu, \phi)$, defined in (6f), depends on the optical properties of cirrus clouds and the underneath "virtual surface." Equation (13) suggests an approach to derive the quantity Γ. To illustrate the method, let us consider an image covering a spatial domain that is sufficiently large for statistical significance whereas it is still small enough for spatial homogeneity (i.e., the spatial variation of Γ due to the variation of solar and view geometry is insignificant). If the image is obtained for homogeneous surface conditions (e.g., in the case over calm ocean surface), i.e., the quantity d in (3) is quasi constant, then the scatterplot of $r_{1.38}(\mu_0, \phi_0, \mu, \phi)$ versus $r_{0.66}(\mu_0, \phi_0, \mu, \phi)$ shows a number of points that are scattered around a straight line, as is illustrated in the left panel of Fig. 2. Note that the parameter d in (13) can be divided into two parts: one is homogeneous for all pixels (e.g., contribution from Rayleigh scattering); the other varies with pixels. The slope of the straight line is essentially the quantity Γ. The interception of the line with the x axis indicates the magnitude of Rayleigh scattering of molecules superimposed with the minimum reflectance of the "virtual surface" below cirrus. The reflectance of the "virtual surface" includes the contribution from aerosol scattering and the surface reflectance. It should be pointed out that the Rayleigh scattering term may be quite complicated, because it may be largely affected by cloud three-dimensional effect [18]. For an image over land, the surface reflectance varies from pixel to pixel. As stated in preceding discussions and evident from (8) and (9), the surface reflection contributes to the apparent reflection observed at the 0.66-μm band, but not to the apparent reflection at 1.38-μm band. Thus, the points of the scatterplot of $r_{1.38}(\mu_0, \phi_0, \mu, \phi)$ versus $r_{0.66}(\mu_0, \phi_0, \mu, \phi)$ are diverse along the x axis or the 0.66-μm band, as shown in the right panel of Fig. 2. The straight line that envelops the data points from the left side is surface reflection free or is for a quasi homogeneous surface; consequently, the slope of the line is the quantity Γ. To determine the line in practice, we divide the whole range of 1.38-μm reflectance into a number of small intervals or bins. For each of the bins, the 0.66-μm band reflectance is sorted in a monotonically increasing manner. Among the sorted points for a given bin, the points that are clustered around the minimum value of 0.66-μm band can be used for constructing the straight line whose slope is the quantity Γ. These points essentially have little surface reflection contamination or have homogeneous

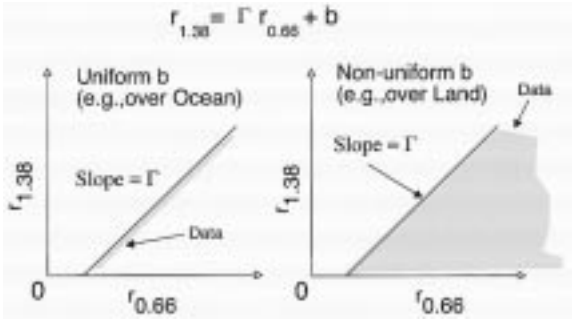

Fig. 2. Conceptual diagram illustrating the derivation of Γ in (12a) and (12b) on the basis of the pixels that correspond to the homogeneous "virtual-surface" condition.

"virtual surface" reflection contributions. We refer these points as the "quasi homogeneous surface" points in this paper.

In practice, we find that a piecewise-linear line with multiple slopes should be used to fit the "quasi homogeneous surface" points. For AVIRIS data, the spatial domain covered by an image is small, and a piecewise-linear line with two slopes can be used, i.e.,

$$x = \begin{cases} a_1 y + b_1, & \text{for } y \in [0, r_{1.38,1}] \\ a_2 y + b_2, & \text{for } y > r_{1.38,1} \\ a_1 r_{1.38,1} + b_1 = a_2 r_{1.38,1} + b_2 \end{cases} \tag{14}$$

where x and y denote apparent reflectances at the 0.66- and 1.38-μm bands, respectively. a_1 and a_2 are $1/\Gamma$ for two regions of the apparent reflectance at the 1.38-μm band, and b_1 is the contribution of Rayleigh scattering due to molecules. The reflectance of cirrus clouds at visible wavelengths is then given by

$$r_c(\lambda, \mu_0, \phi_0, \mu, \phi)\big|_{\lambda \in [0.4,1.0\ \mu\text{m}]} = \begin{cases} a_1 r_{1.38}(\lambda, \mu_0, \phi_0, \mu, \phi), & \text{for } r_{1.38} \in [0, r_{1.38,1}] \\ a_2 r_{1.38}(\lambda, \mu_0, \phi_0, \mu, \phi) + b_2 - b_1, & \text{for } r_{1.38} > r_{1.38,1}, \end{cases} \tag{15}$$

where the effect of Rayleigh scattering has been removed.

For the retrieval of the cirrus reflectance based on MODIS data, we use MODIS Level-1b images [9, p. 79]. The spatial sizes of MODIS Level-1b images are normally about 2800 km $\times$ 2000 km, and a substantial variation of surface reflection condition may exist. To avoid the spatial inhomogeneity, an image must be divided into several subimages for practical retrieval implementation. After carrying out a number of trial-and-error experiments, we found that it is proper to divide a MODIS image into nine subimages to assure retrieval reliability and retain computational economy for massive operational implementation. In addition, a piecewise-linear line with three slopes is required to fit the "quasi homogeneous surface" pixels for each subimage to account for the effect of variations of cirrus cloudy condition, atmospheric profile, and surface feature. The mathematical equations for the piecewise-linear line and the corresponding retrieval result are similar to (14) and (15). However, this approach, which is based on dividing an image into subimages, can lead to "chessboard" effect, i.e., the retrieved cirrus reflectance may be discontinuous at the boundaries of the subimages. To circumvent this shortcoming,

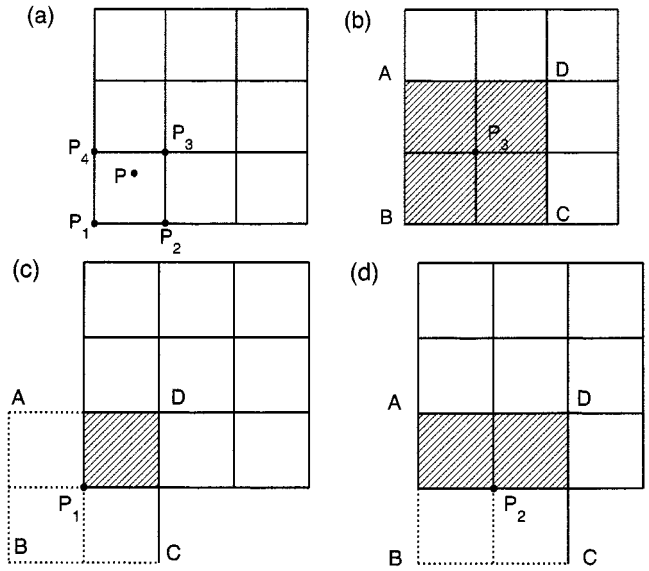

Fig. 3. (a) Division of image into subimages. (b)–(d) Domains defined for the derivation of the piecewise-linear lines corresponding to the homogeneous "virtual-surface" condition. See text for a detailed description.

we apply an interpolation scheme. As shown in Fig. 3(a), let us assume four lines in a three-segment piecewise-linear form, which are obtained from fitting of "quasi homogeneous surface" pixel points, be obtained at four spatial domains centered at P1, P2, P3, and P4. The coordinates for the four points are $(x1, y1)$, $(x2, y1)$, $(x2, y2)$, and $(x1, y2)$. These four lines in a three-segment piecewise-linear format are given by (16), which is shown at the bottom of the page. Furthermore, let the 1.38-μm apparent reflectance at point P be $r_{1.38,P}$. Substituting this value into the four three-segment piecewise-linear lines in (16), we obtain four values for cirrus reflectance at visible wavelengths, as shown in (17) at the bottom of the page. The reflectance of cirrus cloud for pixel P can be given by a two-dimensional interpolation as follows:

$$\begin{aligned} r_{1.38,P} = {} & (1-\alpha)(1-\beta) r_{1.38,P_1} + \alpha(1-\beta) r_{1.38,P_2} \\ & + \alpha\beta r_{1.38,P_3} + (1-\alpha)\beta r_{1.38,P_4} \end{aligned} \tag{18a}$$

where

$$\alpha = \frac{x - x_1}{x_2 - x_1} \text{ and } \beta = \frac{y - y_1}{y_2 - y_1}. \tag{18b}$$

In (18b), x and y are the coordinates of point P. It is important to select the spatial domains for deriving the four three-segment piecewise-linear lines defined in (16). Evidently, the domains must include the point P; otherwise, the resultant three-segment piecewise-linear lines defined in (16) are irrelevant to the spectral information corresponding to pixel P, leading to a meaningless interpolation.

The physical basis for deriving a three-segment piecewise-linear line implies that the pixels in the selected domain are spatially coherent, i.e., for a point located at (x, y) the spatially coherent domain is $(x \pm \Delta x, y \pm \Delta y)$. In the sense that the MODIS Level-1b image is divided into nine subimages, Δx and Δy are the sizes of a subimage in the directions of the along- and cross-satellite orbit track. Thus, for the domain centered at point P_1, the selected spatial domain is region ABCD [shown in Fig. 3(c)]. Note that part of the domain is out of the image; thus, the spectral information from different images is required for deriving the piecewise-linear line for the corner subimage. This substantially complicates the data processing. Additionally, there exist gaps between MODIS images of contiguous orbital tracks. Since the spectral information for regions outside of the areas covered by an image may not be available, we select the region marked with shade in Fig. 3(c) to derive the three-segment piecewise-linear lines for the domain centered at the corner of the image. Similarly, for the spatial domain at the edge of the image, we use two subimages to derive the piecewise-linear line, as is illustrated in Fig. 3(d). For the interior domain, we use four subimages, as shown in Fig. 3(b). In this manner, we can obtain 16 three-segment piecewise-linear lines for an image that is divided into nine subimages. After the 16 three-segment piecewise-linear lines are obtained, the cirrus reflectance for every pixel of the image can be given by the proceeding interpolation scheme. This algorithm has been found to be computationally efficient and stable. With an SGI Octane computer with a 300-MHz timing clock, it takes 1 min for the present retrieval algorithm to process one MODIS Level-1b imaging scene. This retrieval scheme presented here has been fully implemented in

$$x_i = \begin{cases} a_{1,i} y + b_{1,i}, & \text{if } y \in [0, r_{1.38,1,i}] \\ a_{2,i} y + b_{2,i}, & \text{if } y \in (r_{1.38,1,i}, r_{1.38,2,i}] \\ a_{3,i} y + b_{3,i}, & \text{if } y > r_{1.38,2,i} \\ a_{1,i} r_{1.38,1,i} + b_{1,i} = a_{2,i} r_{1.38,1,i} + b_{2,i} \\ a_{2,i} r_{1.38,2,i} + b_{2,i} = a_{3,i} r_{1.38,3,i} + b_{3,i} \end{cases} \quad \text{for } i = 1, \ldots, 4 \tag{16}$$

$$r_{1.38,P_i} = \begin{cases} a_{1,i} r_{1.38,P}, & \text{if } r_{1.38,P} \in [0, r_{1.38,1,i}] \\ a_{2,i} r_{1.38,P} + b_{2,i} r - b_{1,i} r, & \text{if } r_{1.38,P} \in (r_{1.38,1,i}, r_{1.38,2,i}] \\ a_{3,i} r_{1.38,P} + b_{3,i} - b_{1,i} r, & \text{if } r_{1.38,P} > r_{1.38,2,i} \end{cases} \quad \text{for } i = 1, \ldots, 4. \tag{17}$$

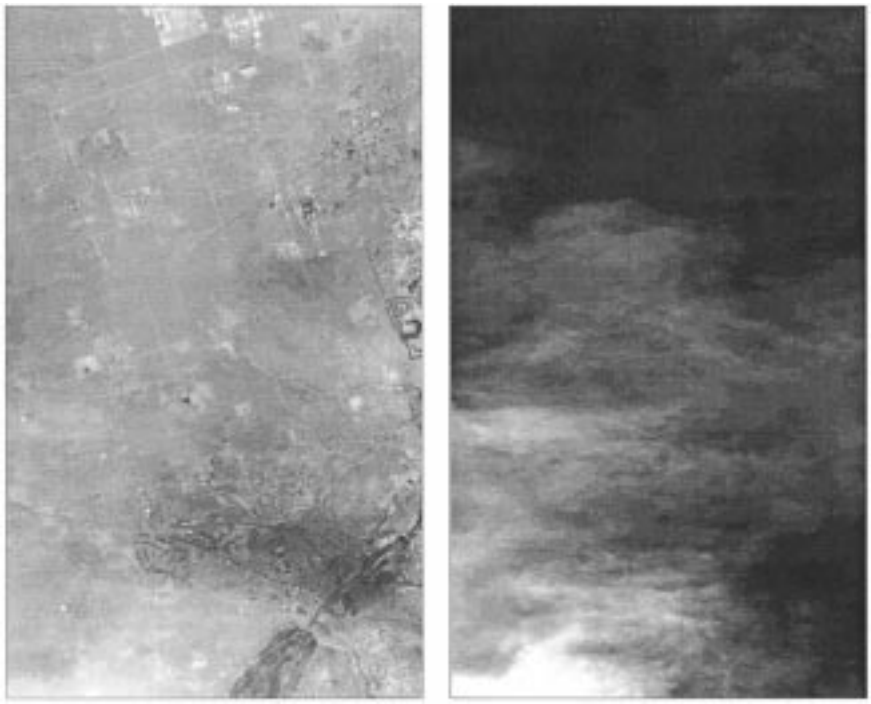

(a) (b)

Fig. 4. (a) AVIRIS 0.66-μm image over Palmdale, California on April 6, 1996. (b) The 1.38-μm image corresponding to the visible image in (a).

the operational MODIS computing environment for deriving the daytime cirrus reflectance at visible wavelengths.

III. Numerical Examples for AVIRIS and MODIS Data

To illustrate the applicability of the retrieval algorithm presented in Section II, we apply this algorithm to AVIRIS and MODIS data. Fig. 4(a) is a combined image of two contiguous AVIRIS images observed at the 0.66-μm band. Note that the regular AVIRIS image size in terms of pixel number is 614×512; thus, the combined image has a size of 614×1024 pixels. The image was obtained at 1:02 p.m. local time on April 6, 1996, over the Palmdale, CA mountain area. The start and stop latitudes for this specific measurement of ER2 aircraft were $34^\circ 48'$ and $34^\circ 30'$; the start- and stop-longitudes are $-118^\circ 20'$ and $-117^\circ 14'$. From Fig. 4(a), surface reflection is evident because the highways and ground constructions are clearly seen. In addition, cirrus clouds are seen at the lower right corner area of the image. However, it is difficult to distinguish the contrast between cloudy pixels and clear pixels.

Fig. 4(b) is the 1.38-μm band image that corresponds to Fig. 4(a). The surface feature is not seen in Fig. 4(b) because of strong absorption by water vapor below cirrus clouds. The spatial distribution of cirrus clouds is clearly seen. It should be pointed out that the thin cirrus clouds that are not discernable in Fig. 4(a) can be distinguished from the background in the 1.38-μm band image; in particular, the fine feature of the spatial distribution of the clouds can be seen in Fig. 4(b).

Fig. 5 shows the scatterplot of the 0.66-μm radiance data shown in Fig. 4(a) versus the 1.38-μm band radiance data shown in Fig. 4(b). The diamond symbols indicate the pixels selected for fitting the two-segment piecewise line that is free of surface reflection or is associated with a homogeneous "virtual-surface"

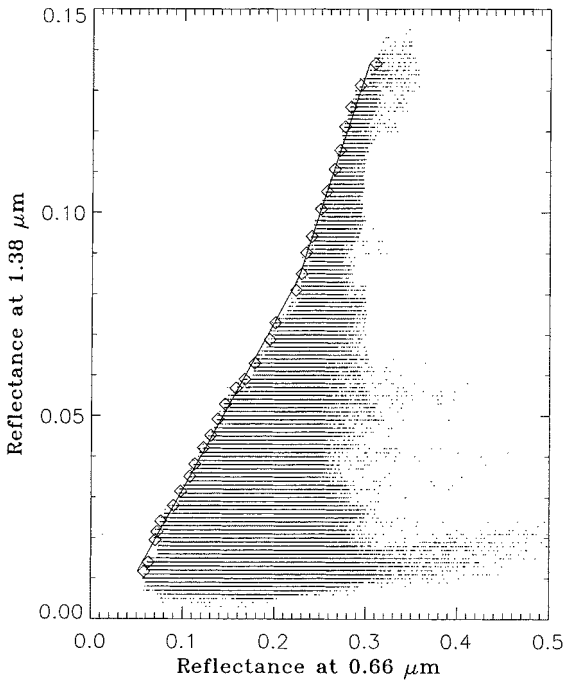

Fig. 5. Scatterplot of 1.38-μm reflectance versus 0.66-μm reflectance corresponding to the two images in Fig. 4(a) and 4(b), respectively.

condition. In this study, instead of using the conventional least square fitting method, we use the robust fitting technique [14] to avoid the sensitivity of the fitted piecewise-linear line to the outliers of the samples. After the two-segment piecewise-linear line is obtained, the cirrus reflectance can be calculated using (15) in a straightforward manner. Fig. 6 shows the retrieved reflectance of cirrus clouds. The maximum value of the reflectance is 0.3. Comparing Figs. 6 and 4(b), one can see that two images are

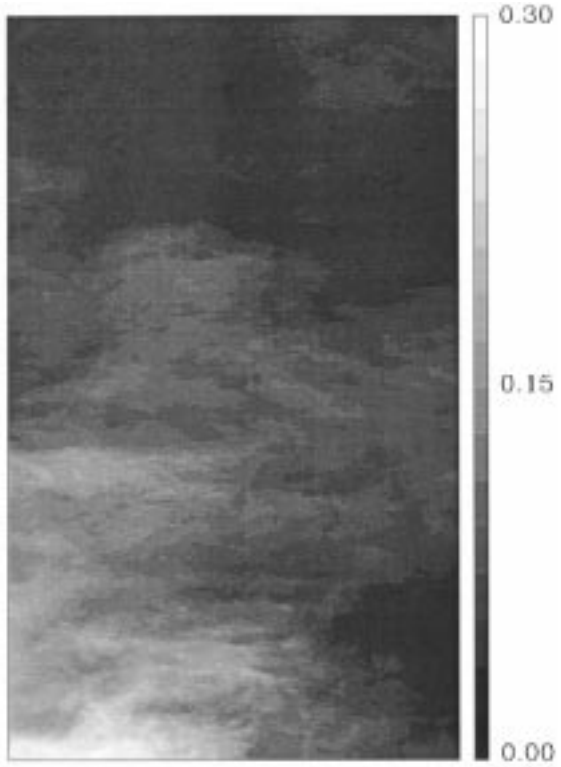

Fig. 6. The cirrus reflectance retrieved on the basis of the spectral information shown in Fig. 4.

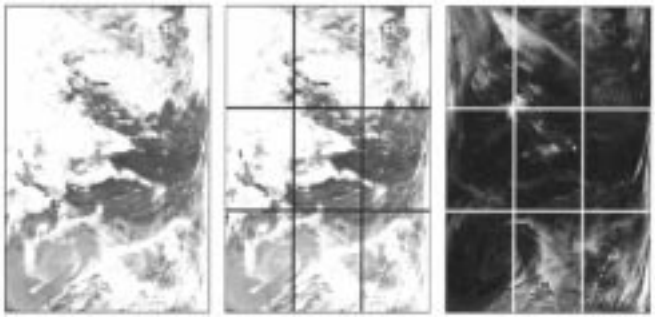

(a) (b) (c)

Fig. 7. (a) 0.55-μm channel MODIS image obtained over Mongolia and the western part of China on 05:05-05:10 UTC, December 1, 2000. (b) 0.66-μm image that corresponds to the 0.55-μm channel image in (a). (c) 1.38-μm image corresponds to the images shown in (a) and (b). Note that the presence of cirrus clouds is evident from the 1.38-μm image, whereas these cirrus clouds are not clearly distinguishable from background in visible channel images.

very similar. This is because the 1.38-μm image displays the spatial distribution of cirrus reflectance, but the magnitude of the reflectance is attenuated by the absorption of water vapor above cirrus clouds. Evidently, the present retrieval algorithm for cirrus reflectance retains the detailed feature of the spatial variation pattern of the cirrus reflection.

Fig. 7(a) is a 0.55-μm band MODIS image obtained over Mongolia and the western part of China on 05:05-05:10 UTC, December 1, 2000. Both cloud and surface features are evident from the image. It is difficult to distinguish high-level cirrus clouds from low-level water clouds from this image. In fact, one can hardly tell the existence of cirrus clouds.

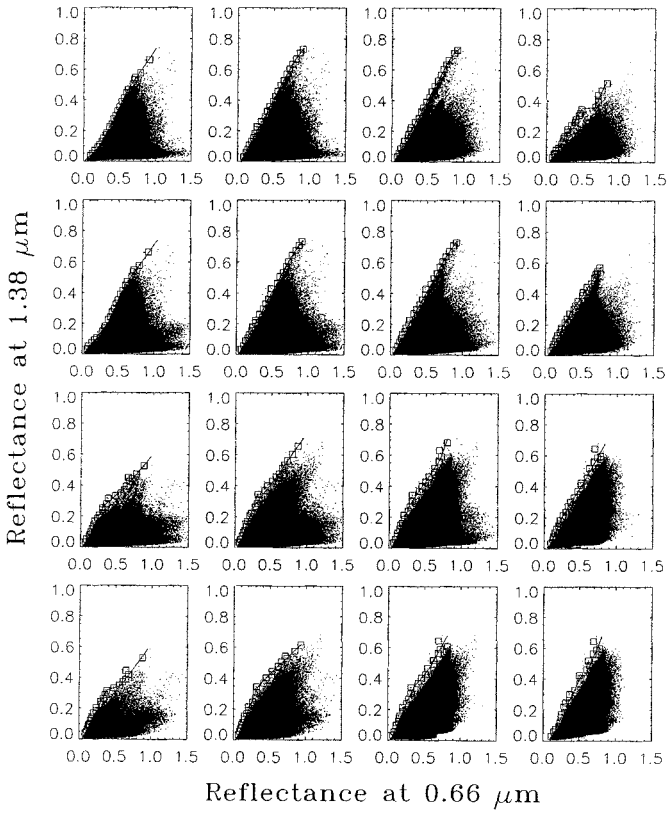

Fig. 8. Scatterplots of 1.38-μm reflectance versus 0.66-μm reflectance, which correspond to the images in Fig. 7(a) and 7(b). Note that 16 scatterplots are shown for the 16 spatial domains centered at the nodes in the division of a MODIS image into nine subimages (see Fig. 3 and the associated context).

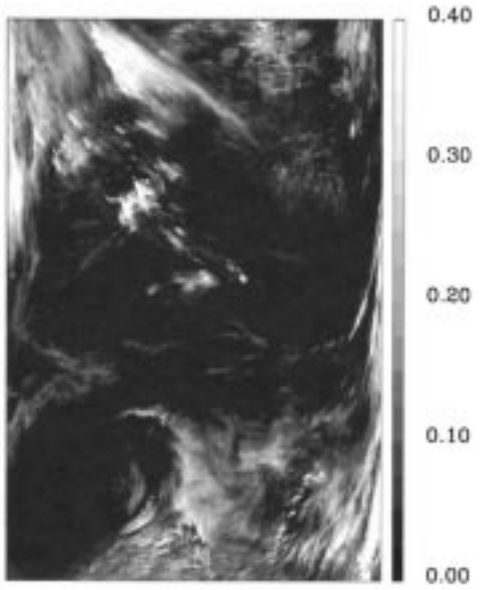

Fig. 9. Cirrus reflectance retrieved using the 0.66-μm and 1.38-μm spectral information shown in Fig. 7(a) and 7(b).

The 0.66- and 1.38-μm images corresponding to Fig. 7(a) are shown in Fig. 7(b) and 7(c), respectively. Note that the entire images in Fig. 7(b) and 7(c) have been divided into nine subimages for the purpose described in Section II. The overall feature of the 0.66-μm band image is similar to the 0.55-μm band

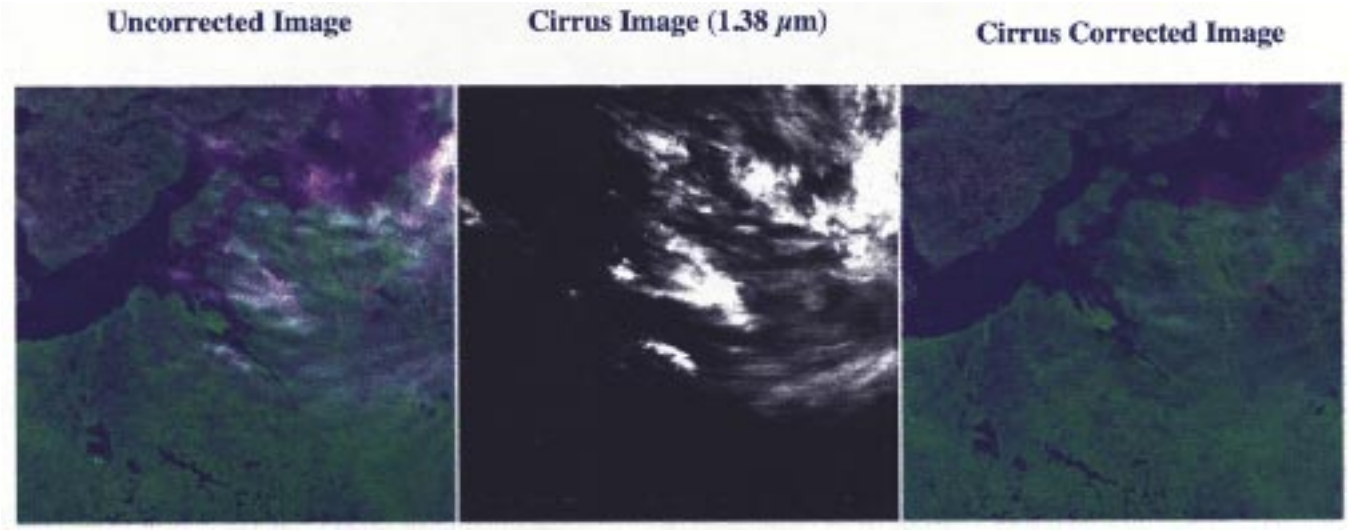

Fig. 10. (a) MODIS RGB (red: 0.66-μm band; green:0.86-μm; and blue: 0.55-μm band) obtained over Victoria Island and Coronation Gulf Dease Strait, northern Canada at 19:15 UTC, September 2, 2000. (b) 1.38-μm image corresponding to RGB image in (a). Note that cirrus clouds are clearly distinguishable. (c) RGB image for which the cirrus contamination has been removed.

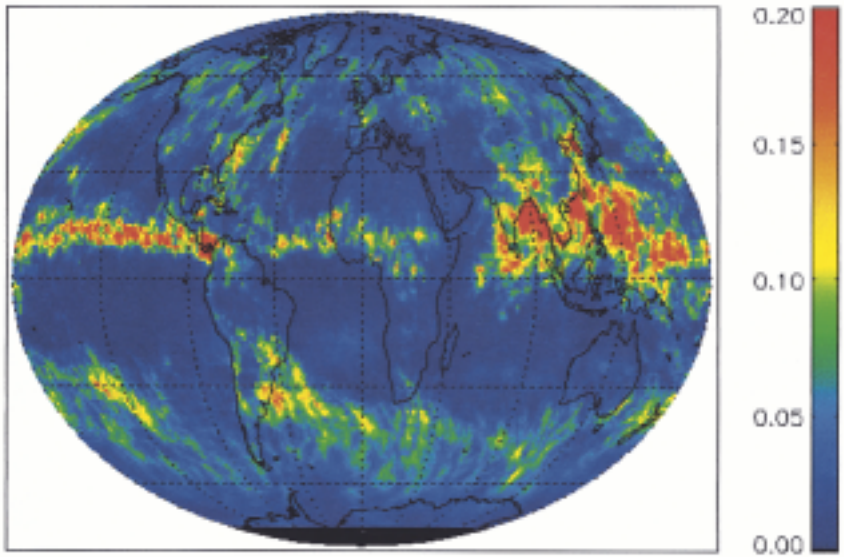

Fig. 11. Monthly-averaged global cirrus reflectance for August 2000. Abundant cirrus clouds are observed over the western Pacific, the Bay of Bengal, as well as the Inter Tropical Convergence Zone in the eastern Pacific Ocean where convection is most active.

image. There is no contrast between the low- and high-cloud pixels. Unlike the 0.66-μm band or the 0.55-μm band images, the 1.38-μm band image clearly shows cirrus clouds that are seen at the upper-left and low-right area of the image domain.

Fig. 8 shows the scatterplot of 1.38-μm band radiance versus 0.66-μm band radiance. The square symbols indicate the pixels that are free of surface reflection or which correspond to a homogeneous surface condition. The three-segment piecewise-linear lines obtained from the fitting of the data indicated by the square symbols are shown. From Fig. 8, it can be seen that the variation range for the 0.66-μm band is much larger than that for the 1.38-μm band.

Fig. 9 shows the cirrus reflectance retrieved using the 16 three-segment piecewise-linear lines shown in Fig. 8 and the 1.38-μm image on the basis (17) and (18a,b). The "chessboard" effect or the discontinuity of the retrieved results at the boundaries of the subimages are not observed. The maximum value of the retrieved cirrus bidirectional reflectance for this image is 0.89. For most pixels, the cirrus reflectance is less than 0.4, which indicates that the cirrus clouds are optically thin.

One of the motivations for retrieving cirrus reflectances is to remove cirrus contamination in satellite images for the study of land or ocean. The left panel of Fig. 10 is a false MODIS RGB image (red: 0.66-μm band; green: 0.86-μm band; and blue: 0.55-μm band) obtained over Victoria Island and Coronation Gulf Dease Strait, northern Canada at 19:15 UTC September 2, 2000. In this image, cirrus contamination is evident. The middle panel of Fig. 10 shows the cirrus image based on 1.38-μm band measurement. After the cirrus reflectance is retrieved using 0.66- and 1.38-μm bands, cirrus effects can be removed, as is shown in the right panel of Fig. 10. Both land and water surface features are seen more clearly in the

cirrus-effect-removed image. Thus, satellite images for which the cirrus contamination has been removed can provide more accurate information about the characteristics of the earth's surfaces.

MODIS is the first satellite instrument with the capability of the 1.38-μm band for cirrus cloud study. Thus, MODIS data provide a unique opportunity to study cirrus clouds on a global scale. With the integration of Level-2 retrieved cirrus reflectance, we can obtain the global distribution of cirrus reflectances. This will be useful for the establishment of an improved global cirrus climatology. As an example of this, we show in Fig. 11 a monthly-averaged global cirrus reflectance image for August 2000. Cirrus clouds are observed over many areas. In particular, abundant cirrus clouds are observed over the western Pacific, the Bay of Bengal, as well as the Inter-Tropical Convergence Zone in the eastern Pacific Ocean where convection is most active.

IV. Discussion and Summary

In this paper, we describe an algorithm to derive the bidirectional reflectance of cirrus clouds using 0.66- and 1.38-μm bands. Both bands are available from AVIRIS and MODIS measurements. We show that the atmosphere-surface system can be viewed as being composed of three layers. According to the fundamental principles of the radiative transfer, we formulate the contributions of the three layers to the bidirectional reflectance observed from space. It is shown that the absorption of low-level water vapor at the 1.38-μm band leads to a negligible contribution of the "virtual surface" to the apparent reflectance observed at this band. Furthermore, we derive the basic mathematical equations for scaling off the water vapor absorption above cirrus clouds at the 1.38-μm band so that the true reflectance of cirrus clouds at visible wavelengths can be revealed.

Two numerical algorithms have been developed for AVIRIS and MODIS data. For the former, the retrieval of cirrus reflectance is straightforward using the scatterplot of 1.38-μm band data versus 0.66-μm band data. For MODIS data, an image needs to be divided into nine subimages, and an interpolation is required to overcome the "chessboard" effect for the retrieved results. Numerical examples are given for AVIRIS and MODIS data. It is shown that the present algorithm can retain the detailed spatial feature of cloud reflection in the retrieved results.

We demonstrate that the retrieved cirrus reflectance can be used to remove cirrus scattering effects in satellite images. The removal of cirrus contamination is important for improving the accuracy of surface reflectance retrievals. Finally, we illustrate that the global MODIS cirrus image can be valuable to our understanding of terrestrial cirrus climatology. We certainly expect that the cirrus reflectance data products obtained from MODIS measurements will have important applications to climate-related research.

References

[1] H. Chepfer, P. Goloub, J. Spinhirne, P. H. Flamant, M. Lavorato, L. Sauvage, G. Brogniez, and J. Pelon, "Cirrus cloud properties derived from POLDER-1/ADEOS polarized radiances: First validation using a ground-based lidar network," *J. Appl. Meterol.*, vol. 39, 2000.

[2] D. R. Dowling and L. F. Radke, "A summary of the physical properties of cirrus clouds," *J. Appl. Meterol.*, vol. 39, pp. 970–978, 1990.

[3] D. Frankel, K. N. Liou, S. C. Ou, D. P. Wylie, and P. Menzel, "Observations of cirrus cloud extent and their impacts to climate," in *Proc. Ninth Conf. Atmospheric Radiation*, Long Beach, CA, Feb. 2–7, 1997, pp. 414–417.

[4] B.-C. Gao, A. F. H. Goetz, and W. J. Wiscombe, "Cirrus cloud detection from airborne imaging spectrometer data using the 1.38 μm water vapor band," *Geophys. Res. Lett.*, vol. 20, pp. 301–304, 1993.

[5] B.-C. Gao and Y. J. Kaufman, "Selection of 1.375 μm MODIS channel for remote sensing of cirrus clouds and stratospheric aerosols from space," *J. Atmos. Sci.*, vol. 52, pp. 4231–4237, 1995.

[6] B.-C. Gao, Y. J. Kaufman, W. Han, and W. J. Wiscombe, "Correction of thin cirrus path radinace in the 0.4–1.0 μm spectral region using the sensitive 1.375 μm cirrus detecting channel," *J. Geophys. Res.*, vol. 103, pp. 32169–32176, 1998.

[7] B.-C. Gao and R.-R. Li, "Quantitative improvement in the estimates of NDVI values from remotely sensed data by correcting thin cirrus scattering effects," *Remote Sens. Environ.*, vol. 74, pp. 494–502, 2000.

[8] M. D. King, Y. J. Kaufman, W. P. Menzel, and D. Tanre, "Remote sensing of cloud, aerosol and water vapor properties from the Moderate Resolution Imaging Spectrometer (MODIS)," *IEEE Trans. Geosci. Remote Sensing*, vol. 30, pp. 2–27, Jan. 1992.

[9] M. D. King, S.-C. Tsay, S. E. Platnick, M. Wang, and K. N. Liou, "Cloud retrieval algorithms for MODIS: Optical thickness, effective particle radius and thermodynamic phase," in *MODIS Algorithm Theoretical Basis Document*: NASA, 1997.

[10] S. Liang and A. H. Strahler, "Retrieval of surface BRDF from multiangle remote sensed data," *Remote Sens. Environ.*, vol. 50, pp. 18–30, 1994.

[11] K. N. Liou, *Radiation and Cloud Process in the Atmosphere: Theory, Observation and Modeling*. New York: Oxford University Press, 1992.

[12] ——, "Influence of cirrus clouds on weather and climate processes: A global perspective," *Mon. Weather Rev.*, vol. 114, pp. 1167–1198, 1986.

[13] K. N. Liou, S. C. Ou, F. P. J. Valero, and T. P. Ackerman, "Remote sensing of the cirrus cloud temperature and optical depth using ER-2 6.5 and 10.5 μm radiometers," *J. Appl. Meteorol.*, vol. 29, pp. 716–726, 1986.

[14] W. H. Press, B. P. Flannery, S. A. Teukolsky, and W. T. Vetterling, *Numerical Recipes*. New York: Cambridge University Press, 1989.

[15] J. H. Seifeld and Clouds, "Contrails and climate," *Nature*, vol. 391, pp. 837–838, 1998.

[16] G. Vane, R. O. Green, T. G. Chrien, H. T. Enmark, E. G. Hansen, and W. M. Porter, "The airborne visible/infrared imaging spectrometer," *Remote Sens. Environ.*, vol. 44, pp. 127–143, 1993.

[17] E. Vermote, D. Tanre, and M. Herman, "Atmospheric effects on satellite imagery: Correction algorithms for ocean color or vegetation monitoring," *Int. Soc. Photogrammetry Remote Sens.*, vol. 28, pp. 46–55, 1990.

[18] G. Wen, R. F. Cahalan, S.-C. Tsay, and L. Oreopoulos, "Impact of cumulus cloud spacing on Landsat atmospheric correction and aerosol retrieval," *J. Geophys. Res.*, vol. 106, pp. 12129–12138, 2001.

[19] B. A. Wielicki, J. T. Shuttles, A. J. Heymsfield, R. M. Welch, J. D. Spinhirne, M.-L. C. Wu, D. O. Starr, L. Parker, and R. F. Arduini, "The 27–28 October 1986 FIRE IFO cirrus case study: Comparison of radiative transfer theory with observations by satellite and aircraft," *Mon. Weather Rev.*, vol. 188, pp. 2356–2376, 1990.

[20] D. P. Wylie and W. P. Menzel, "Eight year of high cloud statics using HIRS," *J. Climate*, vol. 12, pp. 170–184, 1999.

[21] D. P. Wylie, W. P. Menzel, H. M. Wolf, and K. I. Strabala, "Four years of global cirrus cloud statistics using HIRS," *J. Climate*, vol. 7, pp. 1972–1986, 1994.

[22] P. Yang, K. N. Liou, K. Wyser, and D. Mitchell, "Parameterization of the scattering and absorption properties of individual ice crystals," *J. Geophys. Res.*, vol. 105, pp. 4699–4718, 2000.

Bo-Cai Gao received the B.S. degree in physics from Nankai University, Tianjin, China, in 1982, and the M.S. and Ph.D. degrees in physics from The Ohio State University, Columbus, in 1984 and 1988, respectively.

He is currently with the Remote Sensing Division, Naval Research Laboratory, Washington, DC. He is a member of the MODIS Science Team since 1996, where his focus is on the remote sensing of cirrus clouds, atmospheric water vapor, and coastal water.

Dr. Gao received a Prize Paper Award from IEEE Geoscience and Remote Sensing Society (IGARSS) in 1991 for his development of an operational atmospheric radiative transfer code to retrieve surface reflectance spectra from hyperspectral imaging data measured with the NASA/JPL Airborne Visible/Infrared Imaging Spectrometer (AVIRIS).

Ping Yang (M'81–SM'86–F'91) received the Ph.D. degree in meteorology from University of Utah, Salt Lake City, in 1995.

He is currently an Assistant Professor at the Department of Atmospheric Sciences, Texas A&M University, College State. After graduation from the University of Utah, he remained with the university for two year, working as a Postdoctoral Researcher. Later, he was an Assistant Research Scientist at the University of California, Los Angeles, as well as in the Goddard Earth Sciences & Technologies Center/University Maryland Baltimore County, Baltimore, as an Associate Research Scientist. His research interests are in remote sensing and radiative transfer. He has been actively conducting research in modeling of the optical and radiative properties of clouds and aerosols, in particular, cirrus clouds and their applications to space and surface remote sensing.

Wei Han received the B.S. and M.S. degrees in atmospheric physics from Beijing University, Beijing, China, in 1985 and 1988, respectively, and the Ph.D. degree in atmospheric sciences from the University of Alaska, Fairbanks, in 1996.

She is currently a Senior Research Associate at the American Chemistry Society, Washington, DC. After graduation in 1996, she worked at the Remote Sensing Division, Naval Research Laboratory, Washington, DC, as a Research Scientist. Her research work focused on the remote sensing of Arctic clouds, cirrus clouds, atmospheric water vapor, and coastal water.

Rong-Rong Li received the B.S. degree in optical physics from Nankai University, Tianjin, China, in 1982, and the M.S. and Ph.D. degrees in physics from the University of Cincinnati, Cincinnati, OH, in 1989 and 1995, respectively.

She is currently working at the Climate and Radiation Branch of NASA/Goddard Space Flight Center, Greenbelt, MD, through the Science Systems and Applications, Inc., Lanham, MD. She has performed experimental studies on the thermal, electrical, and magnetic properties of commercially available ceramic chips at low temperatures. She has also performed experimental studies on the dynamical properties of two-dimensional superconductor-insulator-superconductor proximity-coupled Josephson junction arrays with different amounts of defects at low temperatures. She is presently analyzing remote sensing data measured with instruments on board aircraft and satellites and is helping with the development of scientific algorithms for retrieving atmospheric aerosol information from data to be acquired with the NASA EOS-MODIS instrument.

Warren J. Wiscombe received the B.S. degree in physics from the Massachusetts Institute of Technology, Cambridge, in 1966, the M.S. degree in physics from the California Institute of Technology (Caltech), Pasadena, in 1966, and the Ph. D. degree in applied mathematics from Caltech in 1970.

He is currently with the Climate and Radiation Branch, NASA Goddard Space Flight Center, Greenbelt, MD. His research interests have included Mie scattering, the DISORT model, the U.S. Department of Energy's Atmospheric Radiation Measurements (ARM) program, radiative transfer in fractal and 3-D clouds, multiple scattering lidars, and revolutionary stratospheric platforms.